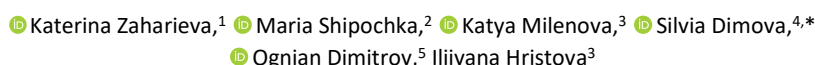


# Photocatalytic UV-Induced Approach for Discoloration of Bromocresol Purple, Bromothymol Blue Dyes and Their Mixture Using $\text{Ni}_x\text{Fe}_{3-x}\text{O}_4/\text{Fe}_2\text{O}_3/\text{AC}$ Composites


 Katerina Zaharieva,<sup>1</sup> Maria Shipochka,<sup>2</sup> Katya Milenova,<sup>3</sup> Silvia Dimova,<sup>4,\*</sup> Ognian Dimitrov,<sup>5</sup> Iliyana Hristova<sup>3</sup>

<sup>1</sup> Institute of Mineralogy and Crystallography “Acad. I. Kostov”, Bulgarian Academy of Sciences, Acad. G. Bonchev St., Block 107, 1113 Sofia, Bulgaria

<sup>2</sup> Institute of General and Inorganic Chemistry, Bulgarian Academy of Sciences, Acad. G. Bonchev St., Block 11, 1113 Sofia, Bulgaria

<sup>3</sup> Institute of Catalysis, Bulgarian Academy of Sciences, Acad. G. Bonchev St., Block 11, 1113 Sofia, Bulgaria

<sup>4</sup> Institute of Polymers, Bulgarian Academy of Sciences, Acad. G. Bonchev St., Block 103A, 1113 Sofia, Bulgaria

<sup>5</sup> Institute of Electrochemistry and Energy Systems “Academician Evgeni Budevski”, Bulgarian Academy of Sciences, Acad. G. Bonchev St., Block 10, 1113, Sofia, Bulgaria

\* Corresponding author’s e-mail address: dimova@polymer.bas.bg

RECEIVED: July 8, 2022 \* REVISED: March 16, 2023 \* ACCEPTED: March 19, 2023

**Abstract:** The nickel ferrite-activated carbon samples  $\text{NiFe}_2\text{O}_4/\text{Activated carbon}$  and  $\text{Ni}_x\text{Fe}_{3-x}\text{O}_4/\text{Fe}_2\text{O}_3/\text{AC}$ ,  $x = 0.25; 0.5$  obtained by co-precipitation followed by thermal treatment in inert atmosphere, were studied for discoloration of Bromocresol Purple (BCP), Bromothymol Blue (BTB) dyes and their mixture as model contaminants under UV-A light. The prepared materials were investigated by XPS, PXRD and XRF analysis, FT-IR spectroscopy, SEM, EDX, BET method and TG analysis.

The photocatalyst with composition  $\text{Ni}_x\text{Fe}_{3-x}\text{O}_4/\text{AC}$ ,  $x = 1$  has demonstrated the highest photocatalytic activity towards discoloration of the BTB in comparison with the others tested materials  $\text{Ni}_x\text{Fe}_{3-x}\text{O}_4/\text{Fe}_2\text{O}_3/\text{AC}$ ,  $x = 0.25; 0.5$ . These results can be explained with the smaller particle sizes, the mesoporous structure, the higher degree of crystallinity and higher content of hydroxyl groups. This study proved that the obtained nickel ferrite-activated carbon materials are suitable as photocatalysts for discoloration of the BTB dye. They have demonstrated also relatively high adsorption ability towards BCP dye.

**Keywords:**  $\text{Ni}_x\text{Fe}_{3-x}\text{O}_4/\text{Fe}_2\text{O}_3/\text{AC}$ , Bromocresol Purple, Bromothymol Blue, mesoporous structure.

## INTRODUCTION

**N** The spinel ferrites with a general formula of  $\text{MFe}_2\text{O}_4$ , are known as magnetic nanoparticles with a spinel structure.<sup>[1]</sup> The spinel crystal structure possesses chemical and thermal stability and improved photocatalytic properties. The nickel ferrite is a compound with narrow band gap (about 1.7 eV) and demonstrated a high photocatalytic activity under visible light.<sup>[2,3]</sup> Nickel ferrite ( $\text{NiFe}_2\text{O}_4$ ) possesses magnetic properties (superparamagnetic, ferrimagnetic, or paramagnetic) depend on its morphology and particle size.<sup>[1]</sup>  $\text{NiFe}_2\text{O}_4$  find applications in catalysis, solid oxide fuel cells, magnetic data storage devices.<sup>[4,5]</sup> Hematite ( $\alpha\text{-Fe}_2\text{O}_3$ ) is an n-type semiconductor and has a band-gap 2.0–2.2 eV. Hematite possesses a chemical

stability, non-toxicity, low cost and abundance.<sup>[6,7]</sup> Hematite has many applications as catalyst, optical properties, for hydrogen production and in water purification.<sup>[6]</sup> Activated carbons (ACs) find application in the field of environmental protection due to their excellent adsorption properties because of their appropriate pore volume and high surface area.<sup>[8]</sup> L. F. Velasco et al.<sup>[9]</sup> show that activated carbon (AC) support (carbon/titania composite) promotes the photodegradation of phenol. The presence of the carbon support enhanced the rate of the process and its chemical and textural properties also have an impact.<sup>[9]</sup>

The increasing of water contamination is mainly due to the human activities leading to the production of wastewater. Various pollutants such as organic and

inorganic compounds, cause water pollution. The dyes are the most complex organic contaminants widely used in the industries. The overuse of dyes causes the existence of the organic wastewater in the environment.<sup>[10]</sup> The photocatalytic degradation is an effective technique for the removal of toxic dyes in a water media.<sup>[11]</sup> The excellent anti-corrosion and magnetic properties, and large surface area of these materials make them attractive for the photocatalytic applications.<sup>[12–16]</sup> The ferrites can easily be separated after photocatalytic processes, due to their magnetic properties and this leads to lower process costs.<sup>[17]</sup>

Photocatalytic degradation of Bromothymol Blue (BTB) in aqueous solutions has been investigated using various photocatalysts as TiO<sub>2</sub>, supported ZnO onto clinoptilolite, CuO, chitosan/magnetite and graphene/chitosan/magnetite nanocomposites, ZnS, CdS and CuS by researchers.<sup>[18–21]</sup>

S. Belattar et al. have studied the decolorization of Bromocresol Purple (BCP) using goethite ( $\alpha$ -FeOOH) as an inducer.<sup>[22]</sup> S. Mohamed Abu El Hassan Mosa has investigated the removal of Bromocresol Purple dye and Carminic Acid from polluted water using silver nanoparticle, ferrous sulfate and H<sub>2</sub>O<sub>2</sub>.<sup>[23]</sup>

Nickel ferrite-based composites are obtained and investigated by various research groups.<sup>[4,7,8,24–28,30,31]</sup> NiFe<sub>2</sub>O<sub>4</sub> nanostructures have been produced using auto-combustion sol-gel route and incorporated with activated carbon as electrode material.<sup>[24]</sup> Nickel ferrite-activated carbon nanocomposite synthesized by hydrothermal method was investigated for selective electrochemical detection of dopamine by T.K. Aparna et al.<sup>[25]</sup> S. I. Moussa et al.<sup>[26]</sup> have obtained activated carbon/NiFe<sub>2</sub>O<sub>4</sub> composite by a precipitation method and applied it for removal of Cu(II), and Zn(II) ions from aqueous solutions. A. C. Fröhlich et al.<sup>[27]</sup> have synthesized NiFe<sub>2</sub>O<sub>4</sub>/activated carbon magnetic composite by hydrothermal method and investigated it as adsorbent to remove the emerging pharmaceutical pollutants ibuprofen and ketoprofen from aqueous solutions. S. Briceño et al.<sup>[28]</sup> have prepared NiFe<sub>2</sub>O<sub>4</sub> supported on activated carbon from petcoke and studied its magnetic properties. Superparamagnetic NiFe<sub>2</sub>O<sub>4</sub> nanoparticles and NiFe<sub>2</sub>O<sub>4</sub>/AC nanocomposite were obtained using the hydrothermal and co-precipitation method by M. J. Livani et al.<sup>[8]</sup> Recently, we have investigated nickel ferrite-activated carbon materials as photocatalysts for degradation of Malachite Green (MG) and Reactive Black 5 (RB5) dyes from aqueous solutions under UV-light. The results have revealed that the degree of degradation of MG dye is higher compared with that of RB5.<sup>[29]</sup> R. Dridi et al.<sup>[4]</sup> deposited on glass substrates NiFe<sub>2</sub>O<sub>4</sub>/ $\alpha$ -Fe<sub>2</sub>O<sub>3</sub> films and tested their photocatalytic activity about the degradation of Methylene Bleu dye under sunlight. Y. Zhang et al.<sup>[7]</sup> have been prepared Fe<sub>2</sub>O<sub>3</sub> nanorod arrays by solvothermal method and in-situ synthesized a hierarchical flower-like nickel

ferrite/hematite heterojunction via facile solution quenched method. The hierarchical magnetic porous  $\gamma$ -Fe<sub>2</sub>O<sub>3</sub>@NiFe<sub>2</sub>O<sub>4</sub> composite with high adsorption efficiency has been synthesized in air by sol-gel auto-combustion method by A.I. Borhan et al.<sup>[30]</sup> Y. Zheng et al.<sup>[31]</sup> have been prepared a charcoal-shaped NiFe<sub>2</sub>O<sub>4</sub>/Fe<sub>2</sub>O<sub>3</sub> electro-Fenton catalyst for degradation of Rhodamine B. NiFe<sub>2</sub>O<sub>4</sub> nanoparticles and a NiO@NiFe<sub>2</sub>O<sub>4</sub> composite have been prepared using hydrothermal method by Y. Zhang et al.<sup>[32]</sup>

Nanosized copper ferrite materials Cu<sub>x</sub>Fe<sub>3-x</sub>O<sub>4</sub>, 0 ≤ x ≤ 1 with different stoichiometries have been synthesized and their photocatalytic activity to the decolorization of Malachite green oxalate under UV irradiation was tested by K. Zaharieva et al.<sup>[33]</sup> Other research groups have been studied many composite structures based on nickel ferrite materials and various transition metal oxides, such as TiO<sub>2</sub>,<sup>[34]</sup> Bi<sub>2</sub>O<sub>3</sub><sup>[35]</sup> etc. Our survey on the available literature concerning the nickel ferrites reveals that the data about the influence of different stoichiometry of NiFe<sub>2</sub>O<sub>4</sub>/AC powders on their structural and photocatalytic properties in the presence of model dyes are incomplete and this fact inspired our present study.

It is known that wastewaters contain admixture from various contaminants. For that reason in our study we performed the photocatalytic experiments using separately BCP or BTB dyes as well as their mixture as model pollutants. The data, observed in the literature concerning the photocatalytic degradation of BCP and BTB dyes are very scarce. We think that investigation of these dyes is environmentally important because they could be release into the waters from manufactures.

The present work deals the preparation and characterization of Ni<sub>x</sub>Fe<sub>3-x</sub>O<sub>4</sub>/AC, x = 1; Ni<sub>x</sub>Fe<sub>3-x</sub>O<sub>4</sub>/Fe<sub>2</sub>O<sub>3</sub>/AC, x = 0.25; 0.5 composites with different stoichiometries. Various physicochemical methods are used to investigate the effect of stoichiometry, structure, morphology and textural characteristics on their adsorption capacity and photocatalytic ability towards UV-induced discoloration of model dyes and their mixture.

## EXPERIMENTAL

### Synthesis of the Nickel Ferrite/Activated Carbon Materials

The Ni<sub>x</sub>Fe<sub>3-x</sub>O<sub>4</sub>/AC, x = 1; Ni<sub>x</sub>Fe<sub>3-x</sub>O<sub>4</sub>/Fe<sub>2</sub>O<sub>3</sub>/AC, x = 0.5; 0.25 (labeled as N1, N2 and N3) materials with different stoichiometry were prepared by the co-precipitation procedure. The initial aqueous solutions of 0.03 M Ni(NO<sub>3</sub>)<sub>2</sub> · 6H<sub>2</sub>O (VWR Prolabo BDH chemicals) and Fe(NO<sub>3</sub>)<sub>3</sub> · 9H<sub>2</sub>O (Alfa Aesar) were mixed in 1:2, 1:5 and 1:11 volume ratios to prepare samples N1, N2 and N3, respectively. Then 2 g of activated carbon (AC) from peach stones (provided by

Laboratory for "Chemistry of Solid Fuels" at the Institute of Organic Chemistry with Centre of Phytochemistry, Bulgarian Academy of Sciences, Bulgaria and the synthesis was described in ref.<sup>[36]</sup> were added to the already prepared solutions mixtures. Water solution of sodium hydroxide (0.3 M, Valerus Co) was added slowly drop by drop into the mixture during continuous stirring. The precipitant was added to pH = 12.5 and after that the mixture was continuously stirred for one more hour. The obtained precipitates were centrifuged and washed with distilled water until neutral reaction medium was reached (pH = 7), after that were dried at 110 °C for 3 hour in air medium. The calcination was carried out at 400 °C for 210 minutes in inert nitrogen atmosphere. The yields of produced samples N1, N2 and N3 are 80 %, 82 % and 82 %, respectively.

### Physicochemical Characterization

The powder X-ray diffraction analysis was performed on a X-ray powder diffractometer "Empyrean" within the range of  $2\theta$  values between 6° and 100° using Co K $\alpha$  radiation ( $\lambda = 0.17902$  nm) at 40 kV. The structural parameters were calculated using the Powder Cell software.<sup>[37]</sup>

The X-ray fluorescence analyses were carried out by WDXRF (Wave-dispersive x-ray fluorescence) Spectrometer Rigaku Supermini 200.

The surface composition and electronic structure were investigated by X-ray photoelectron spectroscopy (XPS). The measurements were carried out on AXIS Supra electron- spectrometer (Kratos Analytical Ltd.) using achromatic AlK $\alpha$  radiation with a photon energy of 1486.6 eV and charge neutralisation system. The binding energies (BE) were determined with an accuracy of  $\pm 0.1$  eV. The chemical compositions in the depth of the films were determined monitoring the areas and binding energies of O1s, Ni2p and Fe2p photoelectron peaks. Using the commercial data-processing software of Kratos Analytical Ltd. the concentrations of the different chemical elements (in atomic %) were calculated by normalizing the areas of the photoelectron peaks to their relative sensitivity factors.

Fourier-transform infrared spectra were collected on Bruker-Vector 22 apparatus in the range of 400–4000 cm<sup>-1</sup>, using KBr pellets.

The morphology of the synthesized nickel ferrite-AC samples was investigated using scanning electron microscope (apparatus JEOL JEM-200CX) at accelerating voltage: 80 keV.

Thermogravimetric analyses (TG) were performed in inert atmosphere on TGA-4000 Perkin Elmer instrument (temperature range 40–800 °C, heating rate of 10 °C / min). The express BET method was applied to measure the specific surface area, based on low-temperature adsorption of nitrogen. The relative error of the method is about 8 %.

The specific surface area and the pore size distribution measurements were carried out on an automated apparatus NOVA Win—CFR Quantachrom—Gas Sorption System. The surface area was calculated using the BET equation, whereupon the pore size distribution and the average pore diameter were evaluated by the DFT method assuming a cylindrical model of the pores. The total pore volume was estimated in accordance with the rule of Gurvich at relative pressure of 0.96. Prior to the measurements, the samples were degassed at 100 °C for 1 hour.

### Photocatalytic Measurements

The photocatalytic discoloration of Bromocresol Purple (BCP), Bromothymol Blue (BTB) dyes and their mixture in ratio 1:1 as model pollutants with initial concentration of aqueous solution of the dye - 7 ppm has been investigated. The synthesized Ni<sub>x</sub>Fe<sub>3-x</sub>O<sub>4</sub>/AC,  $x = 1$ ; Ni<sub>x</sub>Fe<sub>3-x</sub>O<sub>4</sub>/Fe<sub>2</sub>O<sub>3</sub>/AC,  $x = 0.5$ ; 0.25 as photocatalysts were used. The UV-A illumination lamp with maximum emission at 365 nm; 18 W and illumination intensity 2.6 mW cm<sup>-2</sup> was used. The photocatalytic tests were performed in the presence of 1 M HCl acid at pH = 3 and 0.015 M solution of H<sub>2</sub>O<sub>2</sub>. It was proved that the pH value of the model solution has almost no effect on the degradation of BTB dye.<sup>[18]</sup> W. Baran et al.<sup>[38]</sup> established that Bromocresol purple dye degrades better in acidic medium than in alkaline conditions. The photocatalytic measurements were carried out in semi-batch slurry reactor equipped with two frits blowing tiny bubbles of air in order to saturate the solution in dissolved oxygen using 0.15 g photocatalyst and 150 mL of dye solution under constant stirring rate (400 rpm). The tested systems, the dye solution and photocatalyst were stirred in the dark for about 30 min before switching on the UV irradiation for 2 hours in order to reach adsorption-desorption equilibrium state. The investigations of the photocatalytic abilities of Ni<sub>x</sub>Fe<sub>3-x</sub>O<sub>4</sub>/AC,  $x = 1$ ; Ni<sub>x</sub>Fe<sub>3-x</sub>O<sub>4</sub>/Fe<sub>2</sub>O<sub>3</sub>/AC,  $x = 0.5$ ; 0.25 materials were carried out by taking aliquot samples of the suspension out of the reaction vessel after regular time intervals. After that the centrifugation was performed in order to separate photocatalytic sample from the aliquot solution before the UV-Vis spectrophotometric evaluation of the dye concentration, based on previous calibration. Then the photocatalyst powder, together with the aliquot solution, was returned back into the reaction vessel, which ensured operation under constant volume and amount of the photocatalytic powder. The reaction course was monitored by UV-Vis absorbance spectrophotometer UV-1600PC in the wavelength range from 200 to 800 nm ( $\lambda_{\max} = 590$  nm for BCP and  $\lambda_{\max} = 440$  nm for BTB). The apparent rate constants ( $k_{app}$ ) were calculated assuming a pseudo-first-order kinetic reaction:

$$\ln\left(\frac{C_0}{C}\right) = tk_{app} \quad (1)$$

where  $C_0$  and  $C$  are respectively initial concentration before turning on the illumination and residual concentration of the dye solution after illumination in the course of given time interval.

The adsorption capacity of the materials was calculated using the formula (2):

$$Q = \frac{(C_0 - C)V}{m} \quad (2)$$

where  $C_0$  is initial dye concentration,  $C$  is dye concentration after 60 min,  $V$  is solution volume, and  $m$  is sample mass.

## RESULTS AND DISCUSSION

The Powder X-ray diffraction patterns of the synthesized  $\text{Ni}_x\text{Fe}_{3-x}\text{O}_4/\text{AC}$ ,  $x = 1$ ;  $\text{Ni}_x\text{Fe}_{3-x}\text{O}_4/\text{Fe}_2\text{O}_3/\text{AC}$ ,  $x = 0.5$ ;  $0.25$  (N1, N2 and N3) materials and AC are displayed on the Figure 1. The presence of stoichiometric and non-stoichiometric spinel nickel ferrite phase (ICDD-PDF file – 10-0325; PDF file – 73-0603) was established. The hematite phase (PDF file – 89-0599) was also registered in  $\text{Ni}_x\text{Fe}_{3-x}\text{O}_4/\text{Fe}_2\text{O}_3/\text{AC}$ ,  $x = 0.5$ ;  $0.25$  samples N2 and N3. Also was registered peak, corresponding to the carbon phase (PDF file – 56-0160) in materials N1, N2 and N3. The decrease of the intensity of carbon peaks for samples N1-N3 due to the decrease in graphitization degree proves formation of composites between activated carbon and metal oxides.<sup>[39,40]</sup> The calculated average crystallite size, lattice microstrain parameter and unit cell parameter of the spinel ferrite and hematite phases are presented in Table 1. The mean crystallite size of spinel ferrite phase and hematite is about 13.3–14.76 nm and 26.74–29.21nm, respectively.

XPS analysis have been carried out to determine the chemical state and surface composition of the

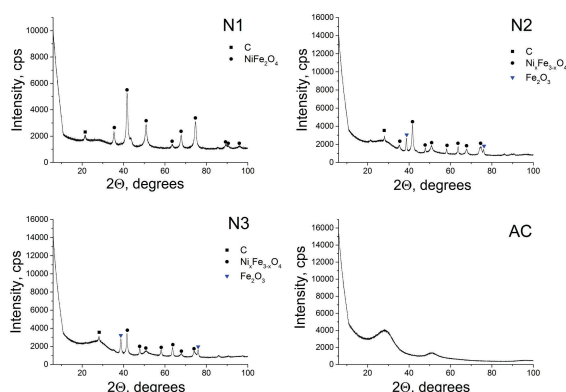


**Figure 1.** PXRD patterns of prepared  $\text{Ni}_x\text{Fe}_{3-x}\text{O}_4/\text{AC}$ ,  $x = 1$ ;  $\text{Ni}_x\text{Fe}_{3-x}\text{O}_4/\text{Fe}_2\text{O}_3/\text{AC}$ ,  $x = 0.5$ ;  $0.25$  (N1, N2 and N3) materials and AC.

$\text{Ni}_x\text{Fe}_{3-x}\text{O}_4/\text{AC}$ ,  $x = 1$ ;  $\text{Ni}_x\text{Fe}_{3-x}\text{O}_4/\text{Fe}_2\text{O}_3/\text{AC}$ ,  $x = 0.5$ ;  $0.25$  (N1, N2 and N3) powders. The data show that spectra of O, Ni and Fe were registered on the sample surface. The O1s peaks are wide and asymmetric and could be deconvoluted into several components. The first one at  $\sim 530.3$  eV is assigned to lattice oxygen in  $\text{Fe}_2\text{O}_3$  and the chemical bond of  $\text{Ni}_x\text{Fe}_{3-x}\text{O}_4$ .<sup>[41]</sup> The second one at  $\sim 531.9$  eV is attributed to iron in conjunction with OH groups. The last two peaks could be attributed to carbon in carbon-oxygen surface adsorbed particles, coming from surface contamination (Figure 2) and water. The low intensity peak at 855.2 eV corresponds to  $\text{NiFe}_2\text{O}_4$  crystalline phase<sup>[42]</sup> (Figure 2). The

**Table 1.** Calculated values of average crystallite size ( $D$ ), lattice strain ( $\epsilon$ ) and unit cell parameter ( $a$ ) of  $\text{Ni}_x\text{Fe}_{3-x}\text{O}_4$  ( $x = 1; 0.5; 0.25$ ) and  $\text{Fe}_2\text{O}_3$  phases of the  $\text{Ni}_x\text{Fe}_{3-x}\text{O}_4/\text{AC}$ ,  $x = 1$ ;  $\text{Ni}_x\text{Fe}_{3-x}\text{O}_4/\text{Fe}_2\text{O}_3/\text{AC}$ ,  $x = 0.5$ ;  $0.25$  (N1, N2 and N3) samples.

Sample	Phase	$D$ / nm	$\epsilon \times 10^{-3}$ / a.u.	$a$ / Å
N1	$\text{Ni}_x\text{Fe}_{3-x}\text{O}_4$ ( $x = 1$ )	13.3	2.59	8.31
N2	$\text{Ni}_x\text{Fe}_{3-x}\text{O}_4$ ( $x = 0.5$ )	14.74	2.75	8.33
	$\text{Fe}_2\text{O}_3$	26.74	2.06	5.01
N3	$\text{Ni}_x\text{Fe}_{3-x}\text{O}_4$ ( $x = 0.25$ )	14.76	2.77	8.34
	$\text{Fe}_2\text{O}_3$	29.21	2.21	5.01

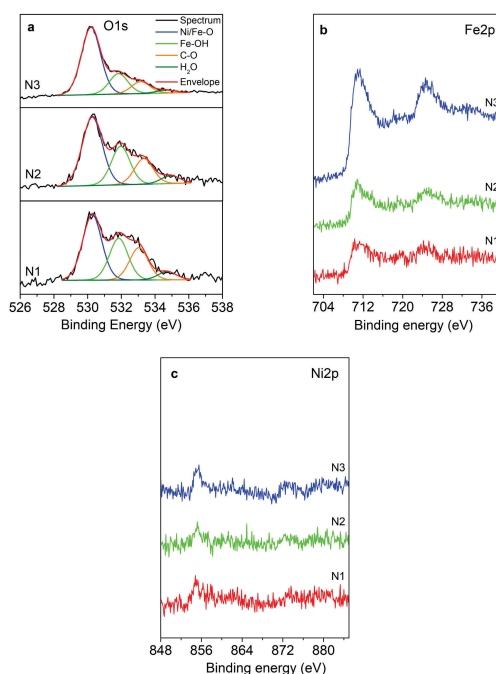


**Figure 2.** Deconvolution of O1s spectra (a) and Fe2p (b) and Ni2p (c) core level spectra  $\text{Ni}_x\text{Fe}_{3-x}\text{O}_4/\text{AC}$ ,  $x = 1$ ;  $\text{Ni}_x\text{Fe}_{3-x}\text{O}_4/\text{Fe}_2\text{O}_3/\text{AC}$ ,  $x = 0.5$ ;  $0.25$  (N1, N2 and N3) powders.



spectra of iron corresponds to  $\text{Fe}_2\text{O}_3$ ,  $\text{Ni}_x\text{Fe}_{3-x}\text{O}_4$ , and  $\text{FeOOH}$  with binding energy at  $\sim 710.2$  eV, 711.1 eV and 712.6 eV (Figure 2). The XPS results for the chemical composition of the powders, given in Table 2 revealed that the sample N2 possess the highest content of Ni ions. This does not correlate with the initial Ni content, due to the fact, that the XPS is surface analysis method (the signal is taken from the surface at a depth of 3–10 nm). The differences in composition between the evaluated by XPS and the initial composition, according to the experimental procedure could be due to the accumulation of Ni ions on surface.

It was established that the sample N1 possesses the largest content of surface OH groups (see Table 2). The surface composition of prepared  $\text{Ni}_x\text{Fe}_{3-x}\text{O}_4/\text{AC}$ ,  $x = 1$ ;  $\text{Ni}_x\text{Fe}_{3-x}\text{O}_4/\text{Fe}_2\text{O}_3/\text{AC}$ ,  $x = 0.5$ ; 0.25 (N1, N2 and N3) materials established by XPS analyses is presented in Table 2.

The XRF study determined the content of Ni (32.9 mass %) and Fe (61.7 mass %) for sample N1; Ni (17.6 mass %) and Fe (76.5 mass %) for sample N2; Ni (8.4 mass

%) and Fe (85.9 mass %) for sample N3. The results from XRF analyses established that the obtained elemental compositions corresponding well with the initial stoichiometric compositions of the prepared samples.

The FT-IR spectra of synthesized samples recorded in the range  $400\text{--}4000\text{ cm}^{-1}$  are shown in Figure 3. The presence of absorption peaks below  $700\text{ cm}^{-1}$  are indication for all ferrites.<sup>[43]</sup> The bands about  $3425\text{--}3443\text{ cm}^{-1}$  corresponding to O–H stretching mode of hydroxyl groups and adsorbed water.<sup>[44]</sup> The absorption bands around  $574\text{--}593\text{ cm}^{-1}$  are associated with the stretching vibration of the tetrahedral metal–oxygen bond and  $410\text{--}477\text{ cm}^{-1}$  corresponding to the metal–oxygen vibrations in octahedral sites.<sup>[43,45]</sup> The band around  $1500\text{--}1600\text{ cm}^{-1}$  could be attributed to the aromatic C=C ring stretching for activated carbon.<sup>[46]</sup> The band at  $1150\text{ cm}^{-1}$  can also be associated with C–O symmetric and asymmetric stretching vibration (–C–O–C– ring).<sup>[47]</sup>

The SEM photographs revealed that the sample N3 possesses ferrite particles with different – irregular shape. The dominate particles size of sample N3 is above 20 micrometers (Figure 4), while the sample N2 possesses smaller particles having size up to 10 micrometer. The porous structure of the activated carbon was also clearly visible. As can be seen, some ferrite particles are situated in the pores and on the surface of activated carbon. The ferrite material with the highest content of nickel ions  $\text{Ni}_x\text{Fe}_{3-x}\text{O}_4/\text{AC}$ ,  $x = 1$  (N1) possess the particles with the smaller size in comparison with the other two samples -  $\text{Ni}_x\text{Fe}_{3-x}\text{O}_4/\text{Fe}_2\text{O}_3/\text{AC}$ ,  $x = 0.5$ , 0.25 (N2 and N3). It has to be noted, that the considerable share of small sized ferrite particles enter into the activated carbon pores. Another

**Table 2.** Concentration of the elements on the surface in at. % by XPS.

sample	O [at.%]	Ni [at.%]	Fe [at.%]	$O_{\text{total}}/O_{\text{hydroxyl groups}}$
N1	82.3	7.3	10.4	3.6
N2	78.2	8.4	13.4	3.9
N3	71.9	5.5	22.6	5.1

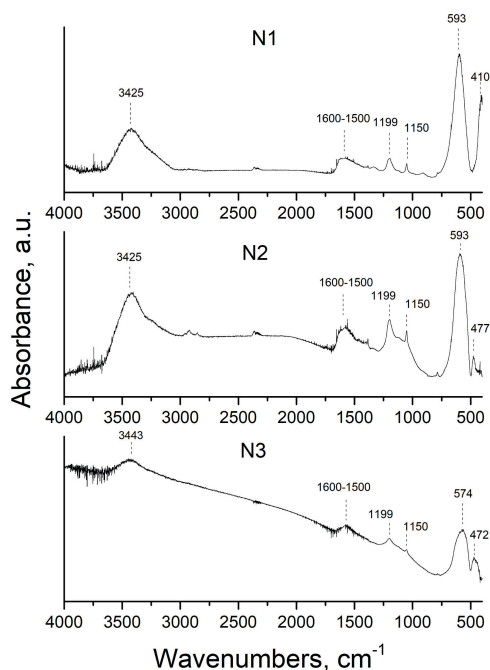


**Figure 3.** FT-IR spectra of prepared  $\text{Ni}_x\text{Fe}_{3-x}\text{O}_4/\text{Fe}_2\text{O}_3/\text{AC}$ ,  $x = 0.25$ ; 0.5 and  $\text{Ni}_x\text{Fe}_{3-x}\text{O}_4/\text{AC}$ ,  $x = 1$  (N3, N2 and N1) samples.

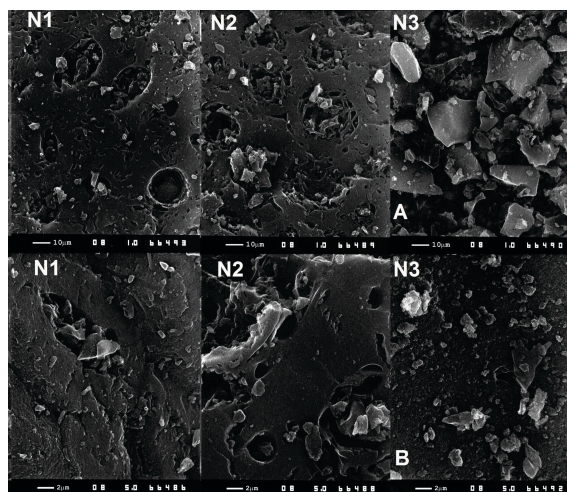


**Figure 4.** SEM pictures of synthesized nickel ferrite-activated carbon powders:  $\text{Ni}_x\text{Fe}_{3-x}\text{O}_4/\text{AC}$ ,  $x = 1$ ;  $\text{Ni}_x\text{Fe}_{3-x}\text{O}_4/\text{Fe}_2\text{O}_3/\text{AC}$ ,  $x = 0.5$ ; 0.25 (N1, N2 and N3) samples at different magnifications: A) 1000 and B) 5000x.

part of these particles remains on the surface of activated carbon. The all samples possess inhomogeneity and the wide range of particle sizes, especially in N3.

On the Figure 5 are shown the EDX spectra and chemical composition of synthesized  $\text{Ni}_x\text{Fe}_{3-x}\text{O}_4/\text{AC}$ ,  $x = 1$ ;  $\text{Ni}_x\text{Fe}_{3-x}\text{O}_4/\text{Fe}_2\text{O}_3/\text{AC}$ ,  $x = 0.5$ ; 0.25 (N1, N2 and N3) samples. The EDX spectra indicate the presence of Ni, Fe, O and C peaks without other elemental contaminations.

The TG curves of the synthesized samples N1-N3 are shown on Figure 6. The weight loss up to 300 °C is attributed to the dehydration of physically and chemically adsorbed water. The weight loss up to 600 °C due to the small quantity of unreacted ions vaporize in their oxide forms.<sup>[48]</sup> The decomposition of activated carbon starts at temperatures above 600 °C.<sup>[8]</sup> The total weight losses were determined to be 24.9 %; 21.8 %; 21.7 % for the samples N1; N2 and N3.

On Figures 7A–10A are presented the adsorption isotherms of the activated carbon and  $\text{Ni}_x\text{Fe}_{3-x}\text{O}_4/\text{Fe}_2\text{O}_3/\text{AC}$ ,  $x = 0.25$ ; 0.5 and  $\text{Ni}_x\text{Fe}_{3-x}\text{O}_4/\text{AC}$ ,  $x = 1$  (N3, N2 and N1). According to the UPAC classification, the isotherms of the

first three samples approach type I, in which the pores are formed between flat plates and are characteristic of layered structures (such as activated carbon), which are weakly interconnected and with different widths. There is no difference in the type of isotherms of samples N3 and N2 compared to that of the initial activated carbon. The hysteresis region is of the H4 type. In the N1 sample there is a change in the type of adsorption isotherm, namely here

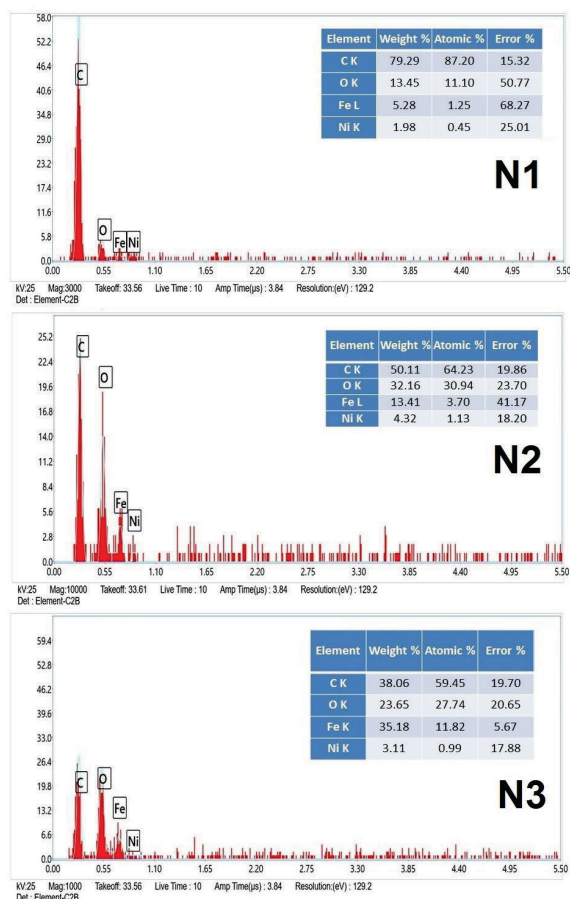


**Figure 5.** EDX spectra and chemical composition of synthesized  $\text{Ni}_x\text{Fe}_{3-x}\text{O}_4/\text{AC}$ ,  $x = 1$ ;  $\text{Ni}_x\text{Fe}_{3-x}\text{O}_4/\text{Fe}_2\text{O}_3/\text{AC}$ ,  $x = 0.5$ ; 0.25 (N1, N2 and N3) samples.

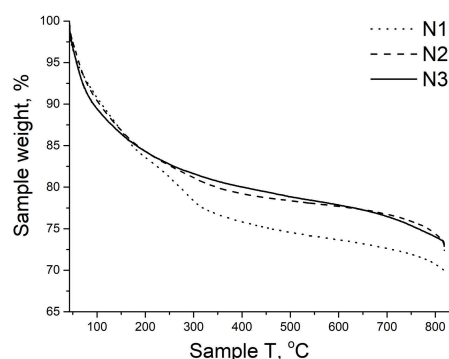


**Figure 6.** TG curves of synthesized  $\text{Ni}_x\text{Fe}_{3-x}\text{O}_4/\text{AC}$ ,  $x = 1$ ;  $\text{Ni}_x\text{Fe}_{3-x}\text{O}_4/\text{Fe}_2\text{O}_3/\text{AC}$ ,  $x = 0.5$ ; 0.25 (N1, N2 and N3) samples.

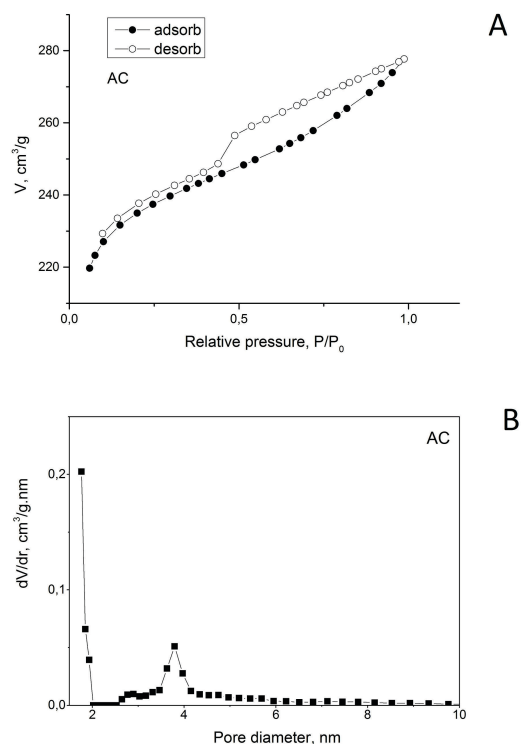


**Figure 7.** A) The nitrogen adsorption-desorption isotherms and B) pore size distribution of activated carbon.

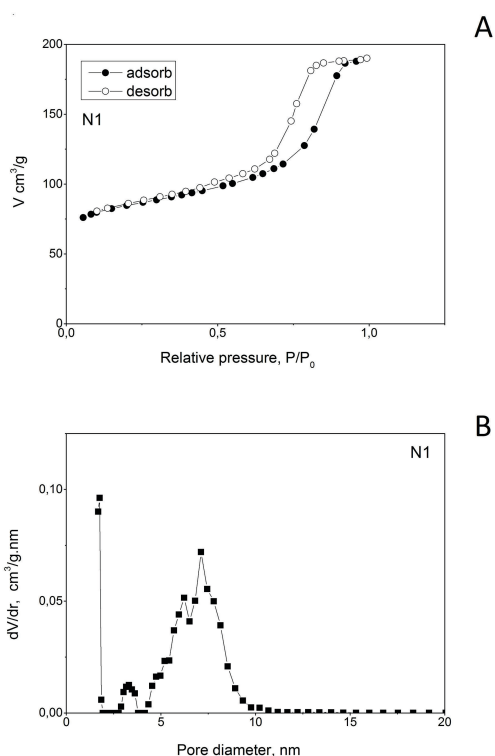


**Figure 8.** A) The nitrogen adsorption-desorption isotherms and B) pore size distribution of synthesized  $\text{Ni}_x\text{Fe}_{3-x}\text{O}_4/\text{AC}$ ,  $x = 1$  (N1) sample.

we are already talking about type VI with hysteresis loop H4 which closes at relative pressures  $P / P_0 < 0.5$ . Broadened hysteresis is an indication not only for the presence of micropores, but also for the increased share of the fine mesopores. A biporous structure was observed, which consists of pores with a size of 3–4 nm and a relatively larger proportion of fine mesopores with sizes from 5 to 10 nm, while the total pore volume remains relatively constant (Table 3). The distribution of the pores of the initial activated carbon associated with an increase in the relative proportion of fine mesopores in the N1 sample is changed, which could be due to the destruction of the carbon texture after thermal treatment (Figure. 7B–10B). The larger amount of metal ions leads to the filling of the pores and the displacement of the maximum number of the

**Table 3.** Textural characteristics of the nickel ferrite-activated carbon materials: specific surface area ( $S_{\text{BET}}$ ), total pore volume ( $V_p$ ) and average pore diameter ( $D_p$ ).

Sample	$S_{\text{BET}} / \text{m}^2 \text{g}^{-1}$	$V_p / \text{cm}^3 \text{g}^{-1}$	$D_p / \text{nm}$
N3	359	0.306	3.4
N2	337	0.3	3.4
N1	265	0.3	4.4
AC	712	0.43	2.4

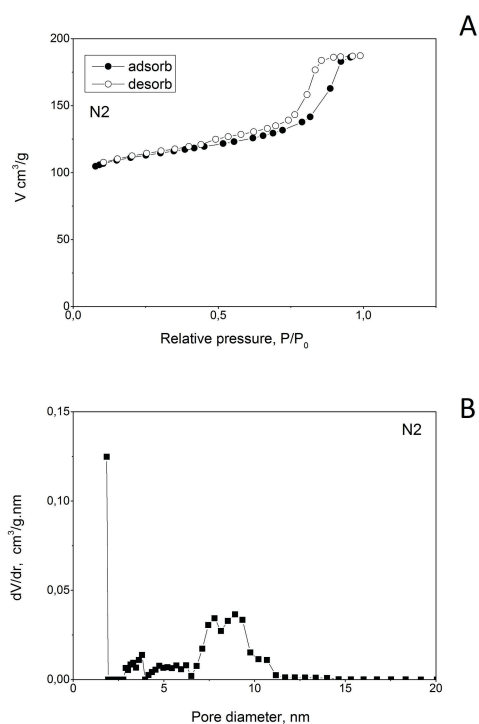


**Figure 9.** A) The nitrogen adsorption-desorption isotherms and B) pore size distribution of synthesized  $\text{Ni}_x\text{Fe}_{3-x}\text{O}_4/\text{Fe}_2\text{O}_3/\text{AC}$ ,  $x = 0.5$  (N2) sample.

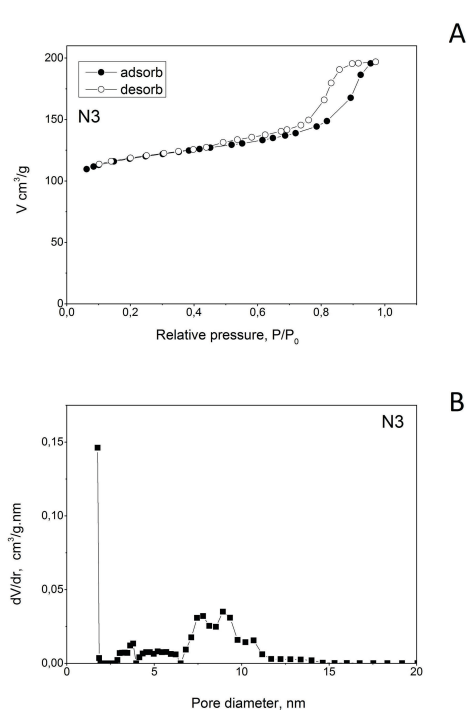


**Figure 10.** A) The nitrogen adsorption-desorption isotherms and B) pore size distribution of synthesized  $\text{Ni}_x\text{Fe}_{3-x}\text{O}_4/\text{Fe}_2\text{O}_3/\text{AC}$ ,  $x = 0.25$  (N3) sample.

mesopores. The experimental data about the texture characteristics are presented in the Table 3. It is clear, that even at low concentrations of metal ions, a significant reduction of the specific surface is observable (sample N3). This is an indication that a process of blocking of the fine mesopores also occurs during the formation of the crystalline phase.

The all results, obtained from XPS, PXRD and XRF analysis, FT-IR spectroscopy, SEM, EDX, TG analysis, nitrogen adsorption-desorption isotherms and BET method about phase composition, elemental composition, structure, morphology, thermal behavior and textural characteristics of synthesized  $\text{Ni}_x\text{Fe}_{3-x}\text{O}_4/\text{AC}$ ,  $x = 1$  and  $\text{Ni}_x\text{Fe}_{3-x}\text{O}_4/\text{Fe}_2\text{O}_3/\text{AC}$ ,  $x = 0.25$ ;  $0.5$  photocatalyst are in agreement.

The photocatalytic discoloration of Bromocresol Purple (BCP), Bromothymol Blue (BTB) dyes and their mixture (volume ratio 1 : 1) were performed using the as-synthesized  $\text{Ni}_x\text{Fe}_{3-x}\text{O}_4/\text{AC}$ ,  $x = 1$ ;  $\text{Ni}_x\text{Fe}_{3-x}\text{O}_4/\text{Fe}_2\text{O}_3/\text{AC}$ ,  $x = 0.5$ ;  $0.25$  powders. Figures 11 and 12 present the concentration changes  $C/C_0$  of BCP and BTB model dyes and their mixture as a function of the time of UV illumination. The photocatalytic tests have revealed that in

the course of the photocatalytic reaction the nickel ferrite-activated carbon photocatalyst  $\text{Ni}_x\text{Fe}_{3-x}\text{O}_4/\text{AC}$ ,  $x = 1$  (N1) leads to the higher degree of discoloration of the BTB dye and their mixture than that of the other two investigated  $\text{Ni}_x\text{Fe}_{3-x}\text{O}_4/\text{Fe}_2\text{O}_3/\text{AC}$  ( $x = 0.5$ ;  $0.25$ ) materials (N2 and N3). All of the investigated nickel ferrite-activated carbon samples have manifested higher photocatalytic efficiency towards BTB degradation. The higher adsorption capacities after 60 minutes time interval, towards BCP dye compared to that of the BTB dye was established (Table 4). Consequently the prepared powders nickel ferrite-activated carbon would be appropriate as adsorbents for BCP dye. The photocatalytic investigations using pure activated carbon demonstrated very low photocatalytic activity towards discoloration of BCP (24 %), BTB (19 %) and their mixture (20 %) in comparison with the prepared composite materials  $\text{Ni}_x\text{Fe}_{3-x}\text{O}_4/\text{AC}$ ,  $x = 1$ ;  $\text{Ni}_x\text{Fe}_{3-x}\text{O}_4/\text{Fe}_2\text{O}_3/\text{AC}$ ,  $x = 0.5$ ;  $0.25$ . The pure  $\text{NiFe}_2\text{O}_4$  and  $\text{Fe}_2\text{O}_3$  discolor BCP (68 %; 35 %), BTB (62 %; 31 %) dyes and their mixture (65 %; 28 %) after 120 minutes UV illumination, respectively. They demonstrate lower photocatalytic ability for discoloration of BCP, BTB and their mixture compared to synthesized composite samples  $\text{Ni}_x\text{Fe}_{3-x}\text{O}_4/\text{AC}$ ,  $x = 1$ ;  $\text{Ni}_x\text{Fe}_{3-x}\text{O}_4/\text{Fe}_2\text{O}_3/\text{AC}$ ,

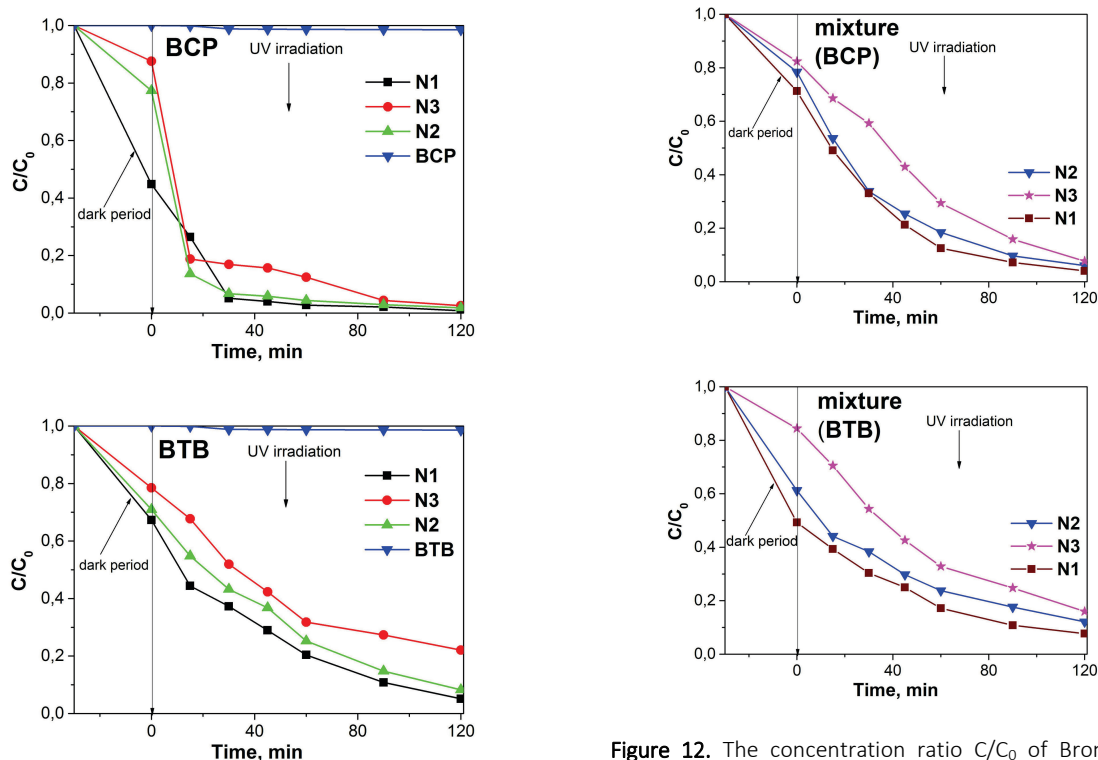


**Figure 11.** The concentration ratio  $C/C_0$  of Bromocresol Purple (BCP), Bromothymol Blue (BTB) dyes with the course of the time of UV illumination using prepared photocatalysts.

**Figure 12.** The concentration ratio  $C/C_0$  of Bromocresol Purple (BCP) and Bromothymol Blue (BTB) dyes mixture with the course of the time of UV illumination using prepared photocatalysts. The values  $C/C$  were evaluated using the corresponding values of the adsorption peaks at 590 nm for BCP dye and 440 nm for BTB dye.

$x = 0.5; 0.25$ . Probably the enhanced adsorption of the dye onto the activated carbon phase followed a transfer through an inter phase to the nickel ferrite phase are responsible for the increased photocatalytic activity of the synthesized composites. Similar synergistic effect in titanium dioxide photocatalyst loaded onto activated carbon support has shown by another research groups.<sup>[49]</sup>

The increased photocatalytic ability of tested nickel ferrite-activated carbon materials with decreasing a particle size of the investigated samples was established. The similar results were obtained by N. Xu et al.<sup>[50]</sup> Surprisingly, the increased specific surface area of the samples with decreasing content of nickel ions, does not result in an increased photocatalytic reaction rate of the studied dyes. Similar results were observed for TiO<sub>2</sub> photocatalytic particles by O. Sheikhejad-Bishe et al.<sup>[51]</sup> The authors have proposed that the imperfect crystallization and the irregular structure are responsible for decreased efficiency of the photocatalyst. Another explanation of these interesting observations could be the filling of the pores of activated carbon with small ferrite particles. These studies show that the investigated nickel ferrite-activated carbon materials are promising photocatalysts due to the high catalytic ability for degradation of Bromothymol Blue dye.

As it can be seen from the Table 4 the photocatalytic activity does not follow the changes of the adsorption capacity. Several research groups have also found that there was no relationship between the dye adsorption and the photocatalytic efficiency of TiO<sub>2</sub> nanoparticles.<sup>[52,53]</sup> It has also to be noted that the tested photocatalysts preserved relatively well their photocatalytic activity after three photocatalytic runs, which indicates their good long-term stability.

Several factors could be responsible for the enhanced activity of Ni<sub>x</sub>Fe<sub>3-x</sub>O<sub>4</sub>/AC,  $x = 1$  (N1): It is known that the smaller size prevents electron-hole pairs recombination and ensures larger number of active sites

for adsorption. The powder Ni<sub>x</sub>Fe<sub>3-x</sub>O<sub>4</sub>/AC,  $x = 1$  (N1) possesses the smallest particle sizes in comparison to the other samples (according to SEM analyses). In addition it was proved for titania photocatalyst, that the recombination pathway could be different for the samples with different particles size.<sup>[54]</sup> The stoichiometric nickel ferrite-activated carbon NiFe<sub>2</sub>O<sub>4</sub>/AC sample (N1) possesses a larger number of active sites available for adsorption of reactive species, due to the larger pore diameter in comparison to the samples N2 and N3, which causes enhanced reaction rate for dye degradation. Bacsa et al. have been revealed the presence of mesopores ensure effective adsorption of the pollutant on the catalyst.<sup>[55]</sup> Similar conclusions concerning the dependence between the pore volume distribution and the photocatalytic activity have been made also by other research groups.<sup>[56,57]</sup> Additional factor, which could influence the photocatalytic activity is the size and number of aggregates. The presence of large number of aggregates in sample N3 decreases the penetration of the light and limits the light scattering. For this reason the sample N3 exhibits lower photocatalytic activity towards both of the dyes in comparison to the other two samples.<sup>[58]</sup> The reaction rate and the mechanism of the photocatalytic process depend also on the amount of surface hydroxyl groups (OH).<sup>[59,60]</sup> The increased amount of hydroxyl groups leads to higher photocatalytic activity TiO<sub>2</sub> samples.<sup>[61-63]</sup> Very recently our research group has been established that this is valid also for ZnO and TiO<sub>2</sub> hydrothermally prepared powders.<sup>[64,65]</sup> By means XPS analyses we have observed for catalyst N1 higher content of surface OH groups, which corresponds with the well-evolved surface and higher number of mesopores in it. The sample N1, which possesses the higher degree of crystallinity (according to PXRD analysis) compared to the others tested photocatalysts N2 and N3. The increased crystallinity of the samples i.e. the decreased amount of bulk defects leads to lower recombination of electron-hole pairs, thus increasing the photocatalytic efficiency of sample N1.<sup>[51,66]</sup>

**Table 4.** Apparent rate constants ( $k$ ) of photocatalytic discoloration of BCP and BTB dyes in aqueous solution under UV light using synthesized photocatalysts and adsorption capacities (mg/g) of the Ni<sub>x</sub>Fe<sub>3-x</sub>O<sub>4</sub>/AC,  $x = 1$ ; Ni<sub>x</sub>Fe<sub>3-x</sub>O<sub>4</sub>/Fe<sub>2</sub>O<sub>3</sub>/AC,  $x = 0.5; 0.25$  (N1, N2 and N3) after 60 minutes.

Dye	BCP	BTB	BCP	BTB
Sample	$k \times 10^{-3} / \text{min}^{-1}$		Adsorption capacities / mg g <sup>-1</sup>	
N1	31.3	20.9	0.129	0.116
N2	25.6	17.9	0.127	0.089
N3	25.3	10.9	0.113	0.105

## CONCLUSIONS

The enhanced photocatalytic activity Ni<sub>x</sub>Fe<sub>3-x</sub>O<sub>4</sub>/AC,  $x = 1$  powders than that of the others tested materials Ni<sub>x</sub>Fe<sub>3-x</sub>O<sub>4</sub>/Fe<sub>2</sub>O<sub>3</sub>/AC,  $x = 0.5; 0.25$  about photocatalytic discoloration of BTB from aqueous solutions under UV irradiation was demonstrated. All of the prepared materials possess the predominantly mesopores structure. The enhanced photocatalytic ability of Ni<sub>x</sub>Fe<sub>3-x</sub>O<sub>4</sub>/AC,  $x = 1$  is due to the higher amount of surface hydroxyl groups, higher degree of crystallinity, smallest particle size and increased relative proportion of fine mesopores in comparison with the other two photocatalysts. The



synthesized separable magnetic materials  $\text{Ni}_x\text{Fe}_{3-x}\text{O}_4/\text{AC}$ ,  $x = 1$ ;  $\text{Ni}_x\text{Fe}_{3-x}\text{O}_4/\text{Fe}_2\text{O}_3/\text{AC}$ ,  $x = 0.5$ ; 0.25 photocatalytic powders manifested high photocatalytic ability towards discoloration of BTB and enhanced adsorption properties to BCP dye. Especially the sample  $\text{Ni}_x\text{Fe}_{3-x}\text{O}_4/\text{AC}$ ,  $x = 1$  could be promising for low cost purification of polluted waste waters.

**Acknowledgment.** The financial support of the National Science Fund, Ministry of Education and Sciences of Bulgaria by Contract DFNI E02/2/2014 is acknowledged. Thanks to Liliya Tsvetanova for her assistance in obtaining the XRF results.

## REFERENCES

- [1] S. A. Jadhav, M. V. Khedkar, S. B. Somvanshi, K. M. Jadhav, *Ceram. Int.* **2021**, *47*, 28623–28633. <https://doi.org/10.1016/j.ceramint.2021.07.021>
- [2] D. Chen, F. Zhang, W. Wang, Y. Yang, G. Qian, *Int. J. Hydrogen Energy* **2018**, *43*, 2121–2129. <https://doi.org/10.1016/j.ijhydene.2017.10.176>
- [3] T. Tatarchuk, B. Al-Najar, M. Bououdina, M. A. A. Ahmed, *Handbook of Ecomaterials* **2018**, 1–50. [https://doi.org/10.1007/978-3-319-48281-1\\_158-1](https://doi.org/10.1007/978-3-319-48281-1_158-1)
- [4] R. Dridi, I. Saafi, A. Mami, A. Amlouk, M. Amlouk, *Surf. Interfaces* **2020**, *21*, 100743. <https://doi.org/10.1016/j.surfint.2020.100743>
- [5] S. B. Narang, K. Pubby, *J. Magn. Magn. Mater.* **2021**, *519*, 167163. <https://doi.org/10.1016/j.jmmm.2020.167163>
- [6] O. Fawzi Suleiman Khasawneh, P. Palaniandy, *Environ. Technol. Innovation* **2021**, *21*, 101230. <https://doi.org/10.1016/j.eti.2020.101230>
- [7] Y. Zhang, J. He, Q. Yang, H. Zhu, Q. Wang, Q. Xue, L. Yu, *J. Power Sources* **2019**, *440*, 227120. <https://doi.org/10.1016/j.jpowsour.2019.227120>
- [8] M. J. Livani, M. Ghorbani, H. Mehdipour, *New Carbon Materials* **2018**, *33*, 578–586. [https://doi.org/10.1016/S1872-5805\(18\)60358-0](https://doi.org/10.1016/S1872-5805(18)60358-0)
- [9] L. F. Velasco, J. B. Parra, C. O. Ania, *Appl. Surf. Sci.* **2010**, *256*, 5254–5258. <https://doi.org/10.1016/j.apsusc.2009.12.113>
- [10] A. Z. Saravani, M. Nadimi, M. A. Aroon, A. E. Pirbazari, *J. Alloys Compd.* **2019**, *803*, 291–306. <https://doi.org/10.1016/j.jallcom.2019.06.245>
- [11] A. Murugesan, M. Loganathan, P. Senthil Kumar, Dai-Viet N. Vo, *Sustainable Chemistry and Pharmacy* **2021**, *21*, 100406. <https://doi.org/10.1016/j.scp.2021.100406>
- [12] M. Z. Khan, I. H. Gul, M. M. Baig, A. N. Khan, *J. Alloys Compd.* **2020**, *848*, 155795. <https://doi.org/10.1016/j.jallcom.2020.155795>
- [13] S. Özçelik, B. Yalçın, L. Arda, H. Santos, R. Sáez-Puche, L. A. Angurel, G. F. de la Fuente, B. Özçelik, *J. Alloys Compd.* **2021**, *854*, 157279. <https://doi.org/10.1016/j.jallcom.2020.157279>
- [14] R. Sharma, P. Thakur, M. Kumar, P. Sharma, V. Sharma, *J. Alloys Compd.* **2018**, *746*, 532–539. <https://doi.org/10.1016/j.jallcom.2018.02.287>
- [15] D. Chahar, S. Taneja, S. Bisht, S. Kesarwani, P. Thakur, A. Thakur, P. B. Sharma, *J. Alloys Compd.* **2021**, *851*, 156878. <https://doi.org/10.1016/j.jallcom.2020.156878>
- [16] M. P. Dojcinovic, Z. Z. Vasiljevic, V. P. Pavlovic, D. Barisic, D. Pajic, N. B. Tadic, M. V. Nikolic, *J. Alloys Compd.* **2021**, *855*, 157429. <https://doi.org/10.1016/j.jallcom.2020.157429>
- [17] G. Mamba, A. Mishra, *Catalysts* **2016**, *6*, 79. <https://doi.org/10.3390/catal606079>
- [18] M. M. Haque, M. Muneer, *Dyes Pigm.* **2007**, *75*, 443–448. <https://doi.org/10.1016/j.dyepig.2006.06.043>
- [19] M. Bahrami, A. Nezamzadeh-Ejehieh, *Mater. Sci. Semicond. Process.* **2015**, *30*, 275–284. <http://dx.doi.org/10.1016/j.mssp.2014.10.006>
- [20] S. Prakash, N. Elavarasan, A. Venkatesan, K. Subashini, M. Sowndharya, V. Sujatha, *Adv. Powder Technol.* **2018**, *29*, 3315–3326. <https://doi.org/10.1016/j.appt.2018.09.009>
- [21] D. Ayodhya, G. Veerabhadram, *J. Sci.: Adv. Mater. Devices* **2019**, *4*, 381–391. <https://doi.org/10.1016/j.jsamd.2019.08.006>
- [22] S. Belattar, N. Debbeche, N. Segharni, T. Sehilli, *Sciences & Technologie A* **2014**, *39*, 49–60.
- [23] S. Mohamed Abu El Hassan Mosa, *International Journal of Advanced Research in Chemical Science* **2014**, *1*, 30–37.
- [24] T. Uzzaman, S. Zawar, M. T. Ansar, S. M. Ramay, A. Mahmood, S. Atiq, *Ceram. Int.* **2021**, *47*, 10733–10741. <https://doi.org/10.1016/j.ceramint.2020.12.189>
- [25] T. K. Aparna, R. Sivasubramanian, *Mater. Today: Proc.* **2018**, *5*, 16111–16117. <https://doi.org/10.1016/j.matpr.2018.05.096>
- [26] S. I. Moussa, M. M. S. Ali, Reda R. Sheha, *Chin. J. Chem. Eng.* **2021**, *29*, 135–145. <https://doi.org/10.1016/j.cjche.2020.07.036>
- [27] A. C. Fröhlich, E. L. Foletto, G. L. Dotto, *J. Cleaner Prod.* **2019**, *229*, 828–837. <https://doi.org/10.1016/j.jclepro.2019.05.037>
- [28] S. Briceño, W. Brämer-Escamilla, P. Silva, J. García, H. Del Castillo, M. Villarroel, J. P. Rodriguez, M. A. Ramos, R. Morales, Y. Diaz, *J. Magn. Magn. Mater.* **2014**, *360*, 67–72. <http://dx.doi.org/10.1016/j.jmmm.2014.01.073>

- [29] K. Zaharieva, K. Milenova, I. Stambolova, V. Blaskov, L. Dimitrov, Z. Cherkezova-Zheleva, A. Eliyas, I. Mitov, *International Scientific Journal "Machines. Technologies. Materials." year X*, **2016**, 5, 10–13.
- [30] A. I. Borhan, D. Gherca, Ş. Cojocaru, N. Lupu, T. Roman, M. Zaharia, M. N. Palamaru, A. R. Jordan, *Mater. Res. Bull.* **2020**, 122, 110664.  
<https://doi.org/10.1016/j.materresbull.2019.110664>
- [31] Y. Zheng, S. Qiu, F. Deng, Y. Zhu, F. Ma, G. Li, *Environmental Technology* **2021**, 42, 1996–2008.  
<https://doi.org/10.1080/09593330.2019.1687586>
- [32] Y. Zhang, W. Zhang, C. Yu, Z. Liu, X. Yu, F. Meng, *Ceram. Int.* **2021**, 47, 10063–10071.  
<https://doi.org/10.1016/j.ceramint.2020.12.153>
- [33] K. Zaharieva, V. Rives, M. Tsvetkov, Z. Cherkezova-Zheleva, B. Kunev, R. Trujillano, I. Mitov, M. Milanova, *Mater. Chem. Phys.* **2015**, 160, 271–278.  
<http://dx.doi.org/10.1016/j.matchemphys.2015.04.036>
- [34] Y. Chen, K. Liu, *Powder Technology* **2017**, 313, 44–53.  
<https://doi.org/10.1016/j.powtec.2017.03.005>
- [35] A. Ren, C. Liu, Y. Hong, W. Shi, S. Lin, P. Li, *Chem. Eng. J.* **2014**, 258, 301–308.  
<http://dx.doi.org/10.1016/j.cej.2014.07.071>
- [36] T. Tsoncheva, B. Tsyntsarski, R. Ivanova, I. Spassova, D. Kovacheva, G. Issa, D. Paneva, D. Karashanova, M. Dimitrov, B. Georgieva, N. Velinov, I. Mitov, N. Petrov, *Microporous Mesoporous Mater.* **2019**, 285, 96–104.  
<https://doi.org/10.1016/j.micromeso.2019.04.051>
- [37] W. Kraus, G. Nolze, *PowderCell for Windows*, Federal Institute for Materials Research and Testing, Berlin, Germany, **2000**.
- [38] W. Baran, A. Makowski, W. Wardas, *Dyes Pigm.* **2008**, 76, 226–230.  
<https://doi.org/10.1016/j.dyepig.2006.08.031>
- [39] H. M. Sabaa, K. M. El-Khatib, M. Y. El-Kady, S. A. Mahmoud, *J. Solid State Electrochem.* **2022**, 26, 2749–2763.  
<https://doi.org/10.1007/s10008-022-05269-w>
- [40] S. Mandizadeh, M. Sadri, M. Salavati-Niasari, *Microporous Mesoporous Mater.* **2018**, 262, 13–22.  
<https://doi.org/10.1016/j.micromeso.2017.11.023>
- [41] P. Li, R. Ma, Y. Zhou, Y. Chen, Q. Liu, G. Peng, Z. Liang, J. Wang, *RSC Adv.* **2015**, 5, 73834–73841.  
<https://doi.org/10.1039/C5RA14713A>
- [42] M. Hua, L. Xu, F. Cui, J. Lian, Y. Huang, J. Bao, J. Qiu, Y. Xu, H. Xu, Y. Zhao, H. Li, *J. Mater. Sci.* **2018**, 53, 7621–7636.  
<https://doi.org/10.1007/s10853-018-2052-7>
- [43] M. A. Gabal, Y.M. Al Angari, *Mater. Chem. Phys.* **2009**, 118, 153–160.  
<https://doi.org/10.1016/j.matchemphys.2009.07.025>
- [44] S. M. Yakout, G. Sharaf El-Deen, *Arabian J. Chem.* **2016**, 9, S1155–S1162.  
<http://dx.doi.org/10.1016/j.arabjc.2011.12.002>
- [45] M. G. Naseri, E. B. Saion, H. A. Ahangar, M. Hashim, A. H. Shaari, *Powder Technology* **2011**, 212, 80–88.  
<https://doi.org/10.1016/j.powtec.2011.04.033>
- [46] C. Saka, *J. Anal. Appl. Pyrolysis* **2012**, 95, 21–24.  
<https://doi.org/10.1016/j.jaap.2011.12.020>
- [47] R. Lapuente, F. Cases, P. Garcés, E. Morallón, J. L. Vázquez, *J. Electroanal. Chem.* **1998**, 451, 163–171.  
[https://doi.org/10.1016/S0022-0728\(98\)00098-9](https://doi.org/10.1016/S0022-0728(98)00098-9)
- [48] G. M. El-Subriti, A. S. Eltaweil, S. A. Sallam, *NANO.*  
<https://doi.org/10.1142/S179329201950125X>
- [49] G. Li Puma, A. Bono, D. Krishnaiah, J. G. Collin, *J. Hazard. Mater.* **2008**, 157, 209–219.  
<https://doi.org/10.1016/j.jhazmat.2008.01.040>
- [50] N. Xu, Z. Shi, Y. Fan, J. Dong, J. Shi, M.Z.-C. Hu, *Ind. Eng. Chem. Res.* **1999**, 38, 373–379.  
<https://doi.org/10.1021/ie980378u>
- [51] O. Sheikhnejad-Bishe, F. Zhao, A. Rajabtabar-Darvishi, E. Khodadad, A. Mostofizadeh, Y. Huang, *Int. J. Electrochem. Sci.* **2014**, 9, 4230–4240.
- [52] M. Uzunova-Bujnova, R. Todorovska, D. Dimitrov, D. Todorovsky, *Appl. Surf. Sci.* **2008**, 254, 7296–7302.  
<https://doi.org/10.1016/j.apsusc.2008.05.331>
- [53] M. Shipochka, A. Eliyas, I. Stambolova, V. Blaskov, S. Vassilev, S. Simeonova, K. Balashev, *Mater. Chem. Phys.* **2018**, 220, 249–259.  
<https://doi.org/10.1016/j.matchemphys.2018.08.054>
- [54] Z. Zhang, Chen-Chi Wang, R. Zakaria, J. Y. Ying, *J. Phys. Chem. B* **1998**, 102, 10871–10878.  
<https://doi.org/10.1021/jp982948+>
- [55] R. R. Bacsa, J. Kiwi, *Appl. Catal. B: Environmental* **1998**, 16, 19–29.  
[https://doi.org/10.1016/S0926-3373\(97\)00058-1](https://doi.org/10.1016/S0926-3373(97)00058-1)
- [56] R. Lamba, A. Umar, S. K. Mehta, S. K. Kansal, *Talanta* **2015**, 131, 490–498.  
<http://dx.doi.org/10.1016/j.talanta.2014.07.096>
- [57] S. Baruah, M.A. Mahmood, M.T. Z. Myint, T. Bora, J. Dutta, *Beilstein J. Nanotechnol.* **2010**, 1, 14–20.  
<https://doi.org/10.3762/bjnano.1.3>
- [58] A. J. Maira, K. L. Yeung, C. Y. Lee, P. L. Yue, C. K. Chan, *J. Catal.* **2000**, 192, 185–196.  
<https://doi.org/10.1006/jcat.2000.2838>
- [59] M. S. Vohra, S. Kim, W. Choi, *J. Photochem. Photobiol., A* **2003**, 160, 55–60.  
[https://doi.org/10.1016/S1010-6030\(03\)00221-1](https://doi.org/10.1016/S1010-6030(03)00221-1)
- [60] H. Park, W. Choi, *J. Phys. Chem. B* **2004**, 108, 4086–4093.  
<https://doi.org/10.1021/jp036735i>
- [61] M. R. Hoffmann, S. T. Martin, W. Choi, D. W. Bahnemann, *Chem. Rev.* **1995**, 95, 69–96.  
<https://doi.org/10.1021/cr00033a004>
- [62] J. Wang, X. Liu, R. Li, P. Qiao, L. Xiao, J. Fan, *Catal. Commun.* **2012**, 19, 96–99.  
<https://doi.org/10.1016/j.catcom.2011.12.028>

- [63] W. Li, D. Du, T. Yan, D. Kong, J. You, D. Li, *J. Colloid Interface Sci.* **2015**, *444*, 42–48.  
<https://doi.org/10.1016/j.jcis.2014.12.052>
- [64] I. Stambolova, V. Blaskov, D. Stoyanova, I. Avramova, K. Milenova, L. Dimitrov, K. Balashev, S. Simeonova, A. Tzonev, L. Alexandrov, A. Eliyas, *Bull. Mater. Sci.* **2017**, *40*, 483–492.  
<https://doi.org/10.1007/s12034-017-1389-x>
- [65] I. Stambolova, D. Stoyanova, M. Shipochka, V. Blaskov, D. Nihtianova, P. Markov, A. Eliyas, R. Mladenova, L. Dimitrov, M. Abrashev, G. Avdeev, K. Zaharieva, *Mater. Charact.* **2021**, *172*, 110775.  
<https://doi.org/10.1016/j.matchar.2020.110775>
- [66] D. Li, H. Haneda, *Chemosphere* **2003**, *51*, 129–137.  
[https://doi.org/10.1016/s0045-6535\(02\)00787-7](https://doi.org/10.1016/s0045-6535(02)00787-7)